Electrohydrodynamics of a current-carrying semi-insulating jet

By J. R. MELCHER AND E. P. WARREN

Department of Electrical Engineering, Massachusetts Institute of Technology

A quasi-one-dimensional non-linear model is developed for the axisymmetric dynamics. Streaming is coaxial with a cylindrical 'wall' supporting a potential having a linear axial dependence. In addition to a tangential field due to an axial current, the stream surface supports charges in proportion to the stream-wall potential difference; hence it is driven by normal and shear electric stresses. Free charge and polarization waves compete with the destabilizing effect of capillarity. With supercritical steady flow (the local jet velocity exceeds the wave velocity), it is found that the stream accelerates or decelerates in accordance with whether an equivalent longitudinal force density is respectively positive or negative. With subcritical flow, the effect of the force is reversed. Experiments demonstrate accelerating and decelerating flow régimes. Model and experiment are in agreement with regard to choking at a critical radius, and the dependence of radius and potential on position. Hysteretic switching between flow régimes is obtained by adjustment of stream and wall potentials, and is explained in terms of the model.

1. Introduction

Droplets of liquid are often produced with the aid of an electric stress. Examples are the particles formed as liquid is drawn from fine capillaries at an elevated potential for use in colloid propulsers (Hogan, Carson, Schneider & Hendricks 1964) and image-making (Heil & Scott 1969). Electrostatic paint spraying equipment makes a similar use of the electric field with the particles sometimes formed at the edge of an electrified sheet (Miller & Spiller 1964). One technique for making particles involves the excitation of capillary instability of a circular jet to pinch off drops of the desired size (Sweet 1964), a process that can be augmented by the addition of a radial electric stress at the interface (Basset 1894; Melcher 1963, p. 123; Taylor 1968). Even though the electric field is exploited as a means of atomizing the fluid, it is well documented that the field can also prevent the formation of particles (Zeleny 1917; Taylor 1969*a*; Carson & Hendricks 1964).

Jets of slightly conducting liquids carrying longitudinal currents are often observed to be free of capillary instability (Taylor 1969*b*). Reports on remarkably long and stable streams in the range of 10^{-5} to 10^{-4} m radius typically describe experiments with fluids conducting as much as glycerine, or even water. The

axial current is conducted to the stream at the orifice, and alternatively returned by means of contact with a downstream electrode, by breakup of the stream into charge-carrying droplets, or through a corona discharge in the neighbourhood of the stream termination.

Even though there are some analogies with the pinch effect of magnetohydrodynamics, it should be recognized that currents are typically in the microampere range, with longitudinal fields of $E \simeq 10^6$ v/m; electro 'static' forces are essential with magnetic fields of negligible significance.
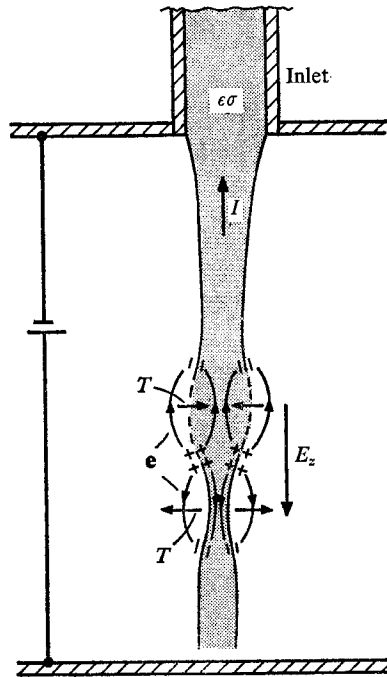

FIGURE 1. Current through a circular cylindrical stream having a relatively short electrical relaxation time is constant; e is the perturbation electric field. A constriction is accompanied by an increase in the local tangential field, hence a polarization restoring surface force which counteracts the destabilizing surface force due to surface tension.

The observed tendency of the field to stabilize some flows can be traced to the relatively high permittivity and conductivity of the streams. For a capillary (sausage) instability on a highly-conducting stream (as illustrated in figure 1), the total steady current I through a given cross-section must be constant. There results a concentration of longitudinal field E_z in the constricted regions. The increased electric field tangential to the interface at the constriction produces an increased outward-directed polarization surface force density T, which tends to restore the equilibrium radius. (The interface of a polarizable fluid in a tangential electric field is drawn toward the region of lesser polarizability.) By contrast with highly insulating fluids (Nayyer & Murty 1960), stabilization of the highly conducting jet depends on distortions of the equilibrium field by

virtue of the stream conductivity, rather than permittivity. The stability is, in part, a matter of the normal stress equilibrium, a view supported by a detailed analysis of the stability for perturbation from an equilibrium wherein there are no electrical shear stresses (Melcher & Schwarz 1968; Saville 1970). What complicates a typical experiment is the equilibrium shear stresses also caused by the electric field. The axial current ensures that the interface is subject to a tangential electric field. If conduction dominates convection, the field interior to the stream is independent of the field constraints in the exterior region. However, the distribution of stream potential determines the distribution of charge on the interface, hence the attendant electric shear stress in the axial direction. The surface charges are distributed in a manner which depends not only on the stream's potential, but on the location of images in the space surrounding the stream: usually determined by the electrodes comprising the stream orifice and sink.

The field surrounding a stream is usually complex, making it difficult to determine the distribution of electrical shear stress, even after the fact.

2. Field and flow configuration

A rational description of the dynamics is made possible by providing for a control of the surface charge distribution on the jet. A cross-section of the experimental configuration is shown in figure 2 (a). The jet, with radius $\xi(z,t)$, is
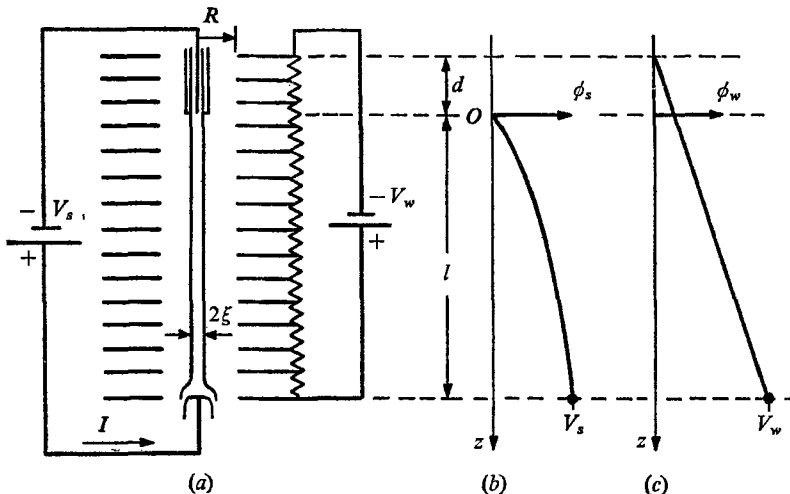

FIGURE 2. (a) Cross-sectional view of stream with control electrodes. (b) Distribution of stream potential. (c) Distribution of wall potential.

ejected from an orifice at $z = 0$ and terminated at $z = l$. A stream potential $\phi_s(z, t)$ is constrained at the extremes of the jet by a potential V_s as sketched in figure 2 (b).

The surface charges are controlled by a 'wall' having a potential $\phi_w(z, t)$ imposed by external sources on washer-shaped electrodes with inner radii R. This constrains the potential exterior to the stream in a manner suggested by

9

previous work (Taylor 1969a). Only sausage (axisymmetric) motions are considered, and therefore, in the long-wave limit, the stream and surrounding wall form coaxial conductors. Although developments hold for a general distribution, attention is concentrated on experiments in which this potential is linear,

$$\phi_w = \frac{V_w(z+d)}{l+d},\tag{1}$$

as sketched in figure 2(c). In the long-wave limit, Gauss's law shows that there is a radial electric field just outside the jet interface given by

$$E_r = \frac{\phi_s - \phi_w}{\xi \ln (R/\xi)};\tag{2}$$

and, because $\epsilon_0 E_r$ is the free surface charge on the stream, it follows that ϕ_w provides a means of adjusting the electrical shear stress.

The electrical shear surface force density T_z is related to ϕ_s and ϕ_w by recognizing that over the jet cross-section,

$$E_z = -\frac{\partial \phi_s}{\partial z},\tag{3}$$

and therefore
$$T_z = \epsilon_0 E_r E_z = -\frac{\epsilon_0 (\phi_s - \phi_w)}{\xi \ln (R/\xi)} \frac{\partial \phi_s}{\partial z}.\tag{4}$$

3. Long-wave model for sausage motions

Quasi-one-dimensional representations of shallow water waves (Stoker 1957) and compressible flows through nozzles and diffusers (Shapiro 1953, p. 73) are a part of the classic literature because they answer questions concerned with flow transition, choking and shock formation, and controlling boundary conditions as related to wave propagation. In the spirit of such models, the jet electrohydrodynamics are formulated using as a starting point the integral laws. The assumption that variations in the jet cross-section occur slowly compared to lengths of interest (typically the distance $R - \xi$), is already implicit in (2)–(4).

A control volume V having fixed incremental length Δz and a deforming, nearly cylindrical surface S, which remains adjacent to the jet interface, is shown in figure 3. Conservation of mass density ρ and charge density q are represented by

$$\frac{\partial}{\partial t} \int_V \rho \, dV + \int_{S_1} \rho \mathbf{v} . \mathbf{n} \, da = 0,\tag{5}$$

$$\frac{\partial}{\partial t} \int_V q \, dV + \int_{S_1} (q\mathbf{v} + \sigma \mathbf{E}) . \mathbf{n} \, da = 0,\tag{6}$$

where S_1 is composed of the two fixed portions of S intersecting the stream and having areas equal to those of the respective cross-sections. It is assumed in the following that the electrical shear stresses are completely transmitted by the internal viscous stresses to the bulk of the fluid, so that the velocity profile,

$\mathbf{v} \simeq v(z,t)\,\mathbf{i}_z$, is constant over a given stream cross-section. It then follows from (5), with S defined to remain just inside the interface, that

$$\frac{\partial}{\partial t}(\rho\pi\xi^2\Delta z) + \|\rho v\pi\xi^2\| = 0, \tag{7}$$

where $\|A\| \equiv A(z+\Delta z) - A(z)$. In the limit $\Delta z \to 0$, we obtain the first of three long-wave equations; for *conservation of mass*,

$$\frac{\partial}{\partial t}\xi^2 + \frac{\partial}{\partial z}(v\xi^2) = 0. \tag{8}$$
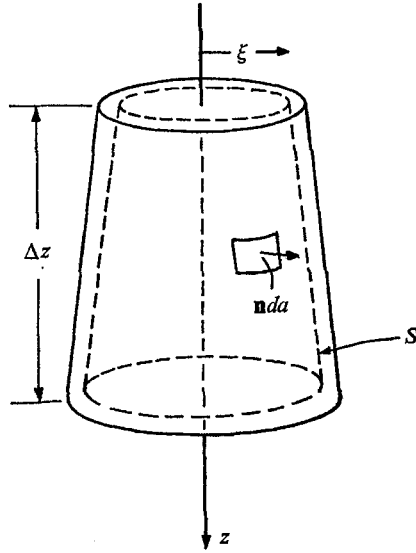

FIGURE 3. Incremental control volume with surface S just inside of the interface.

The second relation follows from (6) wherein S is defined to be just outside the interface. It is recognized that there is no free charge density in the volume of the fluid. Thus, the convection current is due solely to surface charge $\epsilon_0 E_r$, while the conduction is in the volume

$$\frac{\partial}{\partial t}(\epsilon_0 E_r 2\pi\xi\Delta z) + \|\epsilon_0 E_r 2\pi\xi v\| + \sigma\|\pi\xi^2 E_z\| = 0. \tag{9}$$

In the limit $\Delta z \to 0$, with simplifications by virtue of (8), and with the substitution from (2) and (3), a second long-wave equation is obtained; for *conservation of charge*

$$\xi^2\left(\frac{\partial}{\partial t} + v\frac{\partial}{\partial z}\right)\frac{\phi_s - \phi_w}{\xi^2\ln(R/\xi)} - \frac{\sigma}{2\epsilon_0}\frac{\partial}{\partial z}\left(\xi^2\frac{\partial\phi_s}{\partial z}\right). \tag{10}$$

Finally, momentum balance in the axial direction is required. For the volume V, defined now to remain just inside the interface, there are no electrical forces.

The only force contributions are from the pressure p, the viscous stresses T^v, and the gravitational acceleration, taken as acting in the positive axial direction:

$$\frac{\partial}{\partial t}\int_V \rho \mathbf{v}\, dV + \int_{S_1} \rho \mathbf{v}(\mathbf{v}.\mathbf{n})\, da = -\oint_S p\mathbf{n}\, da + \int_V \rho g \mathbf{i}_z\, dV + \oint_S \mathsf{T}^v.\mathbf{n}\, da. \quad (11)$$

For the control volume of figure 3, (11) becomes

$$\frac{\partial}{\partial t}\left(\rho v \pi \xi^2 \Delta z\right) + \|\rho v^2 \pi \xi^2\| = -\|p\pi\xi^2\| + p\frac{\partial \xi}{\partial z} 2\pi\xi\Delta z + \rho g\pi\xi^2\Delta z$$

$$+ T_{zr}^v \left(2\pi\xi\Delta z\right) + 2\mu\pi\|\xi^2\frac{\partial v}{\partial z}\| - 2\mu\frac{\partial v}{\partial z}\left(2\pi\xi\Delta z\right)\frac{\partial\xi}{\partial z}. \quad (12)$$

The first term on the right comes from the component of pressure acting in the axial direction on the almost vertical surface of S. The last two terms are due, respectively, to the normal viscous stresses acting over the stream cross-sections and over the surface next to the interface. The limit is now taken as $\Delta z \to 0$ and the conservation of mass expression, (8), is used to write

$$\rho\xi^2\left[\frac{\partial}{\partial t} + v\frac{\partial}{\partial z}\right]v = -\xi^2\frac{\partial p}{\partial z} + \rho g\xi^2 + T_{zr}2\xi + 2\mu\xi^2\frac{\partial^2 v}{\partial z^2}. \quad (13)$$

Pressure balance at the interface relates p to the quasi-one-dimensional variables. In terms of the Maxwell stresses, the pressure jump at the interface is

$$p_0 - p_s = \tfrac{1}{2}\epsilon_0 E_r^2 - \frac{(\epsilon_0 - \epsilon)}{2} E_z^2 - \frac{\gamma}{\xi}, \quad (14)$$

where p_0 is the ambient pressure of the surroundings (presumed to have negligible mass, hence constant pressure), and γ is the surface tension. In view of (2) and (3), (14) becomes

$$p_0 - p = \tfrac{1}{2}\epsilon_0 \frac{(\phi_s - \phi_w)^2}{\xi^2 \ln^2(R/\xi)} + \frac{\epsilon - \epsilon_0}{2}\left(\frac{\partial\phi_s}{\partial z}\right)^2 - \frac{\gamma}{\xi}. \quad (15)$$

In (13), T_{zr} is T_z as given by (4,) because we presume that the viscous shear stresses at the interface are held in balance by the electrical surface force density. Substitution of (15) and (4) into (13) gives the third equation for the long-wave model: for *conservation of momentum*,

$$\rho\left(\frac{\partial}{\partial t} + v\frac{\partial}{\partial z}\right)v = \frac{\partial}{\partial z}\left[\frac{\epsilon_0(\phi_s - \phi_w)^2}{2\xi^2 \ln^2(R/\xi)} + \frac{(\epsilon - \epsilon_0)}{2}\left(\frac{\partial\phi_s}{\partial z}\right)^2 - \frac{\gamma}{\xi}\right]$$

$$+ \rho g - \frac{2\epsilon_0(\phi_s - \phi_w)}{\xi^2 \ln(R/\xi)}\frac{\partial\phi_s}{\partial z} + 2\mu\frac{\partial^2 v}{\partial z^2}. \quad (16)$$

The quasi-one-dimensional model is summarized by (8), (10) and (16): ϕ_w is prescribed and v, ξ, and ϕ_s are the variables dependent on (z,t).

4. Non-linear wave propagation and domains of influence

The propagation of disturbances is essential to understanding even the steady flow equilibria of the jet, and is considered in this section without the complication of viscous dissipation and a finite electrical relaxation time. This latter condition,

that ϵ_0/σ is short compared to times of interest, reduces (10) to its last term, which is then integrated to obtain

$$\frac{\partial \phi_s}{\partial z} = \frac{I}{\sigma \pi \xi^2}.\tag{17}$$

That is, with charge accumulation on the jet surface ignored in accounting for continuity of conduction current, the total axial current $I(t)$ is independent of z. With the last term in (16) ignored, equations (8), (16) and (17) are three first-order equations having characteristic equations found in the usual manner (Shapiro 1953, p. 73).

$$dv \mp (2a/\xi)\,d\xi = g^*\,dt\tag{18}$$

on lines in the $z-t$ plane such that

$$\frac{dz}{dt} = v \pm a,\tag{19}$$

where
$$a = \left\{ \frac{\epsilon_0}{2\rho\xi^2} \frac{(\phi_s - \phi_w)^2}{\ln^2(R/\xi)}[1 - \ln^{-1}(R/\xi)] + \frac{\epsilon - \epsilon_0}{\rho \pi^2}\left(\frac{I}{\sigma}\right)^2 \frac{1}{\xi^4} - \frac{\gamma}{2\rho\xi} \right\}^{\frac{1}{2}},\tag{20}$$

$$\rho g^* = \rho g - \frac{\epsilon_0 (\phi_s - \phi_w)}{\pi \xi^4 \ln(R/\xi)}\left(\frac{I}{\sigma}\right)\left(2 - \frac{1}{\ln(R/\xi)}\right) - \frac{\epsilon_0(\phi_s - \phi_w)}{\xi^2 \ln^2(R/\xi)}\frac{\partial \phi_w}{dz},$$

and
$$d\phi_s = \frac{I}{\sigma \pi \xi^2}\,dz\tag{21}$$

on lines of constant t.

We are mainly interested here in cases with the stream potential constrained at the orifice and a downstream electrode,

$$\phi_s(0, t) = 0, \quad \phi_s(l, t) = V_s,\tag{22}$$

and so $I(t)$ is whatever it must be, at each instant in time, to satisfy the boundary conditions of (22) and (21) integrated over the stream length.

Given initial values $v = v(z, 0)$ and $\xi = \xi(z, 0)$, the initial value of ϕ_s is determined by (21) and (22). The velocity and radius an instant dt later are determined by (18) and (19), together with boundary conditions consistent with causality. If the flow is subcritical ($v < a$), one upstream and one downstream condition are required. For supercritical flow ($v > a$), two upstream conditions control. In either case, the boundary conditions on (21) hold.

An initial pulse on the stream propagates with wave-fronts defined by the characteristic lines of (19). However, through the instantaneous adjustment of the current throughout the stream, the scale of a disturbance, as well as the slopes of the characteristic lines, are continually being adjusted so that in an average way the dynamics at one position instantaneously influence those at another. With this proviso, we are justified in thinking of wave-fronts propagating along the characteristic lines defined by (19). Implicit to our argument is the assumption that a^2 is positive, so that the characteristics are real. With the electrical excitations small, a^2 is necessarily negative, because of the surface tension; the stream is subject to capillary instability. In the following discussions, the régime $a^2 < 0$ is assumed part of the supercritical régime, with the implied

upstream boundary conditions. Implicit is the assumption, supported by experimental observations, that the capillary instability manifests itself as a growth in space rather than with time.

The three terms of (20) represent the mechanisms for wave propagation. The first term is due to the electrical stresses normal to the stream surface, which (for $\phi_s - \phi_w$ constant) decrease with an increase in the stream radius because of the $1/r$ dependence of the radial electric field. The second term in (20) is due to the polarization force acting in concert with the electrical conduction as described in the introduction. The last term accounts for surface tension and always tends to produce instability. For long waves, an increase in electrical excitations is tantamount to increasing the wave velocity, while surface tension slows the waves.

From perturbation theory, we know that the stabilizing role of electrical normal stresses and the destabilizing effect of surface tension are reversed at short wavelengths (Melcher 1963, p. 123). With a longitudinal wave-number k, these 'self-field' effects come into play for waves having $k\xi \simeq 1$: our long-wave model is restricted to $k\xi \ll 1$ and even more $kR < 1$.

5. Steady flow

5.1. *Flow régimes*

With $\partial/\partial t = 0$, the mass rate of flow Q becomes an invariant along the stream: (8) is integrated to become

$$v = Q/\pi\xi^2. \tag{23}$$

Note that, given Q, we have specified an upstream boundary condition. With (17) and (23) and the observation that $\rho v \partial v/\partial z = \partial(\tfrac{1}{2}\rho v^2)/\partial z$, the inviscid steady form of (16) is

$$\frac{d\xi}{dz} = \frac{\rho g^*}{2\rho\xi^{-1}[a^2 - v^2]}; \quad v^2 = Q^2/\pi^2\xi^4. \tag{24}$$

The integral of this first-order equation must satisfy a second upstream or a downstream boundary condition, depending on whether $v^2 > a^2$ or $v^2 < a^2$. Remember that ρg^* and (a) depend on ϕ_s as well as ξ, and hence solution requires the simultaneous integration of (21), with boundary conditions of (22). The numerator of (24) can be thought of as a net longitudinal force density due to gravity and the electrical shear stresses. Knowledge of the numerator and denominator in (24) is tantamount to knowing the local behaviour of the stream. For the denominator, observe that

$$2\rho\xi^{-1}(a^2 - v^2) = \left\{\frac{2}{\pi^2\xi^5}\left[(\epsilon - \epsilon_0)\left(\frac{I}{\sigma}\right)^2 - Q^2\rho\right] + \frac{\epsilon_0}{\xi^3}\frac{(\phi_s - \phi_w)^2}{\ln^2(R/\xi)}[1 - \ln^{-1}(R/\xi)] - \frac{\gamma}{\xi^2}\right\}. \tag{25}$$

If we think of the difference $(\phi_s - \phi_w)$ in stream and wall potentials as known, then (25) typically depends on stream radius as sketched in figure 4.

We distinguish three possibilities. First, if $(\epsilon - \epsilon_0)(I/\sigma) < Q^2\rho$ and $\phi_s - \phi_w$ is not too large, the denominator is everywhere negative and a monotonically increasing function of ξ, is sketched in figure 4(a). The flow is everywhere supercritical. A positive ρg^* makes $d\xi/dz$ negative, and gives rise to a decreasing radius.

Second, with $(\epsilon - \epsilon_0)(I/\sigma) > Q^2\rho$ and $\phi_s - \phi_w$ yet small, the denominator of (24) is positive for $\xi < \xi_c$, corresponding to subcritical flow, or negative if $\xi > \xi_c$ and the flow is supercritical as shown by figure 4(b). With $\rho g^* > 0$ and supercritical conditions, the radius decreases and the denominator tends to make the rate of
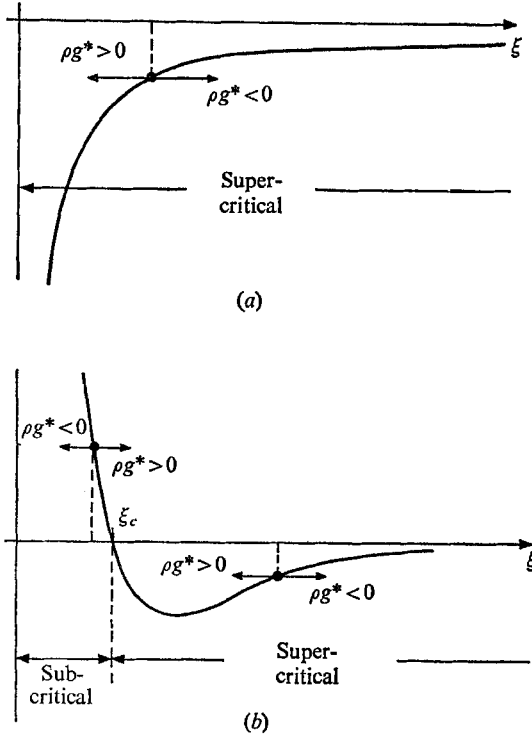

FIGURE 4. The denominator of (24) sketched as a function of stream radius for
(a): $(I/\sigma)^2 < Q^2\rho/(\epsilon - \epsilon_0)$; (b): $(I/\sigma)^2 > Q^2\rho/(\epsilon - \epsilon_0)$.

change smaller. Then the denominator reverses its trend and precipitously approaches zero as $\xi \to \xi_c$. At this critical radius, the slope approaches infinity and we expect that the flow chokes. If $\phi_s - \phi_w$ is sufficiently large, the denominator of (24) can reverse sign twice as ξ is varied, but because this case is found not to be a likely one, it is not discussed. The four possible situations are summarized by figure 5.

The choking phenomenon is unusual. In a supercritical flow, with $\rho g^* > 0$, the stream accelerates toward the critical radius and a subcritical condition. If the material velocity increases, it might be supposed that the flow becomes more supercritical. However, in order for there to be a critical radius, the polarization wave velocity (in the absence of surface tension) must exceed the material velocity, and the flow is supercritical only because the destabilizing effect of surface tension diminishes the total wave velocity to less than the jet velocity. As the stream becomes smaller, the relative effect of surface tension decreases, while conservation of mass and current makes the material and polarization

wave velocities increase to the same degree. Thus, the stream accelerates, but nevertheless approaches the subcritical condition.

The critical radius is determined by (25) set equal to zero, and is presented in figure 6. Without electrical excitations, a^2 is negative and there is no critical radius. If the local $(\phi_s - \phi_w)$ is maintained at zero as I is raised, then a local critical radius obtains as

$$\left(\frac{I}{\sigma}\right)^2 > \frac{Q^2 \rho}{\epsilon - \epsilon_0}. \tag{26}$$
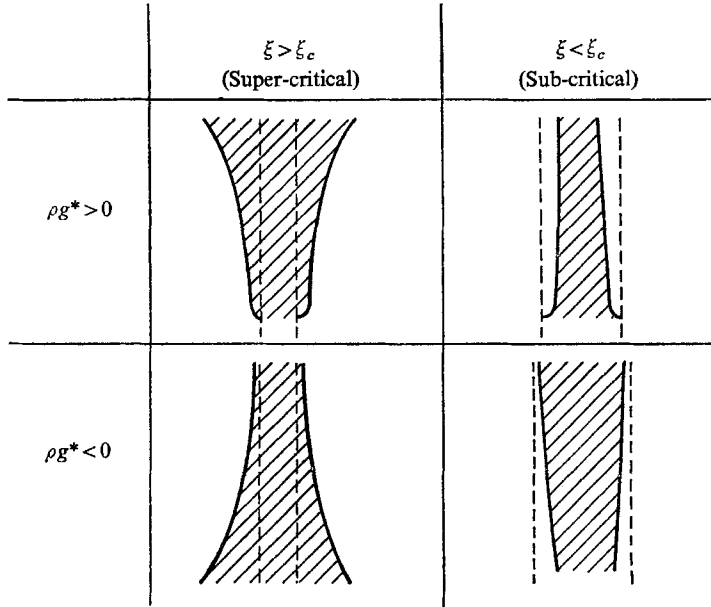

FIGURE 5. Summary of the local flow régimes. - - - - -, critical radius.

The critical radius is zero at the condition of (26), and then increases in value as I is raised further. The wave velocity can be further increased by raising $(\phi_s - \phi_w)^2$, so that a critical radius, as illustrated by the broken curve of figure 6, may exist for values of I somewhat less than those required to satisfy (26). Note that (26) is in any case a sufficient condition to guarantee that a critical radius exists.

5.2. *Supercritical and positive ρg^**

Laminar flow from a downward-directed water spigot is a limiting case of the supercritical $\rho g^* > 0$ flow with no critical radius: one that we know accelerates. However, as we now see, the acceleration is as much a consequence of the supercriticality as it is of the acceleration of gravity. (If it were possible to obtain subcritical flow from a water faucet, we would see a stream which fattens.)

It is also the supercritical, $\rho g^* > 0$ régime, that has probably most often been observed with the longitudinal current. A typical stream is shown in figure 7, with the experiment arranged as depicted by figure 2. There is no experimental offset distance d; orifice and wall are grounded at $z = 0$.

A critical radius does not exist for the experimental conditions of figure 7 (plate 1). Choking of the supercritical, $\rho g^* > 0$, flow plays no apparent role in transitions to other flow régimes for the given conditions. The model represented by (17) and (24) gives a satisfactory representation of the steady flow. A comparison of the results of a numerical integration and the experimental profile shown in figure 7 is illustrated in figure 8. Consistent with the supercritical condition, the upstream radius is used as the second mechanical boundary condition,
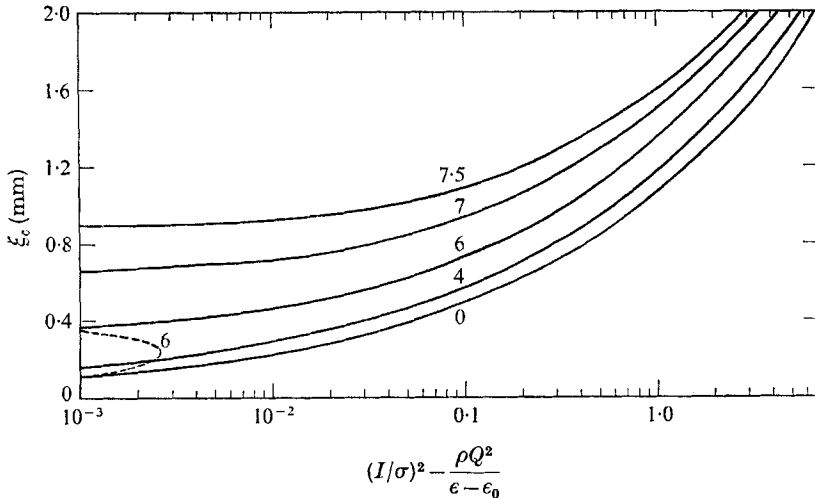

FIGURE 6. Critical radius as it depends on a function representing the current and flow rate. The stream-wall potential difference in kV is the parameter and the curves are the same, whether that parameter is positive or negative. The broken line is for negative $(I/\sigma)^2 - \rho Q^2/(\epsilon - \epsilon_0)$.

with parameters as summarized in the figure caption. In the entrance region, the fringing fields have an influence not accounted for by the long-wave model. However, it is found that the entrance radius has little effect on the theoretical curve of figure 8, as might be expected, since there is little electric stress in the entrance region where the jet is extremely thick. The stream and wall potentials are included with figure 8, and show that the region wherein both $\phi_s - \phi_w$ (the surface charge) and $d\phi_s/dz$ are large is midway between the ends. The experimental potential shown is measured by using the photograph and known total current and voltage.

The stream tends to become uniform for two reasons. As the potentials of the stream and wall approach each other at the downstream end, the electrical shear stress falls to zero. At the same time, the magnitude of the denominator of (24) is increasing rapidly as the radius becomes small, and these effects combine to make $d\xi/dz$ become small. The electrical contributions to ρg^* are dominant over much of the length; at the middle of the jet, the second term in (21) exceeds the first by a factor of more than 200.

As the flow rate is decreased, a threshold is observed below which the steady flow equilibrium is lost; the jet is unstable, and breaks up before it can 'strike'

to the lower electrode. The instability involves both the normal stress considerations described in connection with figure 1 and the equilibrium shear stress. The perturbation dynamics are the subject of work to be reported subsequently.
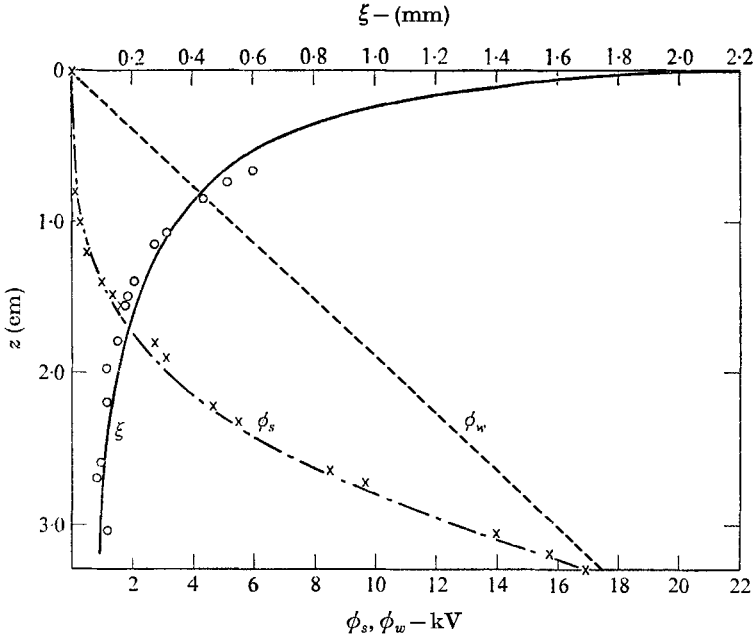

FIGURE 8. Jet radius ξ and potential ϕ_s as a function of longitudinal distance z. ○, ×, data points taken from figure 7(a); ———, — · — · —, obtained from the numerical integration of (17) and (24). Data measured and used in the computation are:

$$Q = 1{\cdot}73 \times 10^{-7} \text{ m}^3/\text{sec}, \quad V_s = 17 \text{ kV}, \qquad V_w = 17{\cdot}5 \text{ kV}, \quad I = 0{\cdot}72 \,\mu\text{ amp},$$

$$\sigma = 1{\cdot}7 \times 10^{-5} \text{ mhos/m}, \quad l = 3{\cdot}3 \text{ cm}, \qquad \gamma = 6{\cdot}34 \times 10^{-2} \text{ nt/m},$$

$$\xi(0) = 2{\cdot}2 \times 10^{-3} \text{ m}, \qquad \rho = 1{\cdot}26 \times 10^3 \text{ kg/m}^3, \quad \epsilon = 42{\cdot}5\epsilon_0, \qquad R = 7{\cdot}95 \text{ mm}.$$

5.3. *Subcritical and positive ρg^**

A second type of transition from the supercritical $\rho g^* > 0$ flow is made if V_s is increased to slightly exceed V_w. Then, there is a dramatic disruption of the accelerating flow of figure 7, replaced immediately by the decelerating flow of figure 9 (plate 2). This régime now persists even if V_s is again decreased somewhat below V_w. In terms of (V_s, V_w), the flow is hysteretic.

To which of the two decelerating flow régimes shown in figure 5 does this case belong? It is reasonable to suppose that ρg^* is now negative, because with $V_s > V_w$, positive surface charges are induced on the lower extremity of the stream, and since I is still positive, the electrical shear stress tends to retard the motion. In fact, the new equilibrium has a retarding electrical shear stress spread over most of its length. Even so, $\rho g^* > 0$ and the flow is subcritical, not supercritical: a view supported by several arguments.

The observed radius apparently is less than the critical radius. Even though the stream radius is greatly increased, the critical radius has increased even more, because I jumps from the $0{\cdot}3$–$0{\cdot}7\,\mu$amp to the 7–$40\,\mu$amp range in the transition.

Figure 10 shows the experimentally observed stream radius just above the lower electrode, as a function of I/σ. The current is increased by increasing the stream potential V_s. For a given family of data, the difference $V_s - V_w$ is then kept constant. In any case, there is little dependence of the stream radius on these low stream-wall potential differences. The radii measured are the largest: upstream, the
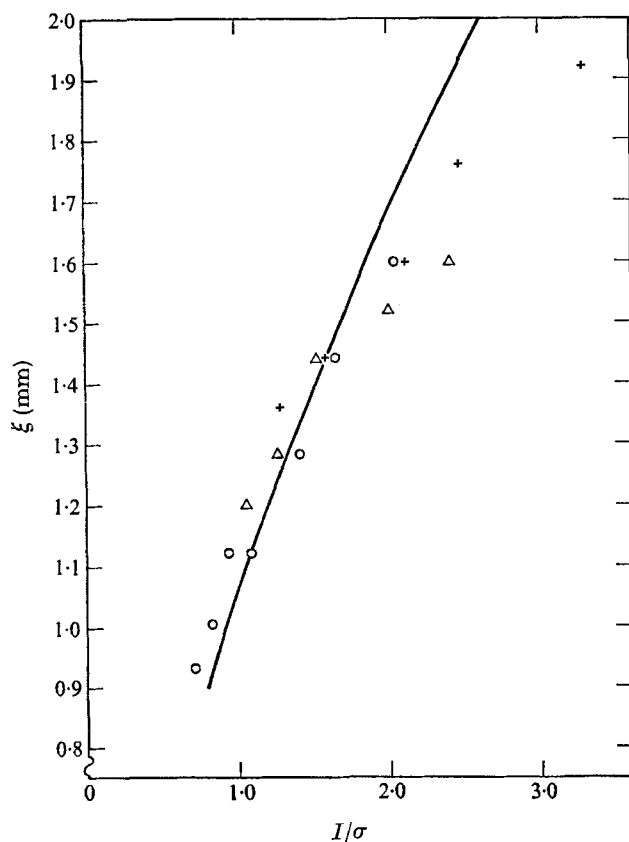

FIGURE 10. Radius of decelerating stream near exit as a function of current for three potential differences between stream and wall at the exit. V_s is typically varied from 13 to 15·5 kV to obtain the variation in current. ——, the theoretical critical radius with $V_s = V_w$. $\bigcirc$, $(V_s - V_w) = 0$, $\triangle$, $(V_s - V_w) = 500$ V; $+$, $(V_s - V_w) = 1000$ V.

radius is less than that shown. The solid line is the critical radius and is essentially the same curve for the values of $V_s - V_w$ in the cases shown. Within experimental errors, the stream radius at the base is the critical radius, and the stream is less than the critical radius over its length.

The downstream radius is a somewhat increasing function of the downstream electrode radius, but if larger electrodes are used, a point is reached at which only a more abrupt change in the radius is obtained as the jet encounters the electrode. The critical radius is apparently an upper limit on the stream radius at the downstream end. This is consistent with the subcritical $\rho g^* > 0$ flow régime of figure 5, wherein the second boundary condition is at the downstream

end. As the stream is forced to approach critical radius, the slope $d\xi/dz$ approaches infinity (see equation (24)).

In this decelerating flow régime, the stream is remarkably uniform and therefore of approximately the critical radius over its length. This is possible only if the electrical shear stresses very nearly balance the gravitational acceleration. Not only is the denominator of (24) nearly zero, but so also is the numerator. We can solve the equation $\rho g^* = 0$, (20), for $(\phi_s - \phi_w)$ to obtain

$$\phi_s - \phi_w = \frac{\rho g}{\epsilon_0} \left\{ \left(\frac{I}{\sigma}\right) \frac{[2 - \ln^{-1}(R/\xi)]}{\pi \xi^4 \ln(R/\xi)} + \frac{d\phi_w}{dz} \frac{1}{\xi^2 \ln^2(R/\xi)} \right\} \tag{27}$$

as the stream-wall potential difference required to maintain a uniform profile. An example is shown in figure 11 for the data given in the caption. The data
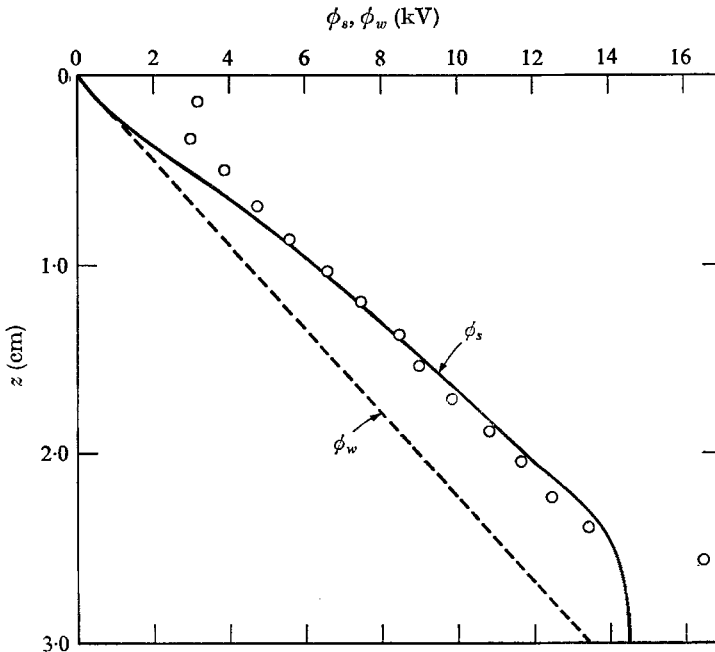

FIGURE 11. ——, the measured stream potential inferred from figure 9. $\bigcirc$, based on the assumption that the numerator in (24) vanishes at each point, so that the potential difference $\phi_s - \phi_w$ is given by (28). Experimental conditions are: $V_w = 13\cdot5$ kV, $V_s = 14\cdot5$ kV, $I = 33\cdot5\,\mu A$, $Q = 1\cdot0 \times 10^{-7}$ m^3/sec, $\sigma = 2\cdot2 \times 10^{-5}$ mhos/m, $R = 7\cdot95$ mm and $l = 3$ cm.

points are based on (27) evaluated using the experimentally determined stream radii, wall potential, and I/σ. This potential profile is to be compared to the solid curve, which is the measured potential distribution based on the experimentally determined stream geometry and current. Over most of the jet, ρg^* is indeed very nearly zero. As might be expected, fringing fields disturb this balance at distances on the order of R from the ends. At those positions where the data points fall above the stream potential, $\rho g^* > 0$. A few points fall slightly below the curve, but by an amount less than the experimental error. Again, the suggestion is that the flow is subcritical.

Because of the entrance fields, evidenced by figure 11, the quasi-one-dimensional model does not hold in the vicinity of the orifice. In fact, because $\phi_s - \phi_w = 0$ at $z = 0$, there is no electrical shear stress there. The stream at first necks down until its potential has risen above that of the adjacent wall, and then the shear stresses take over to produce the essentially uniform equilibrium.
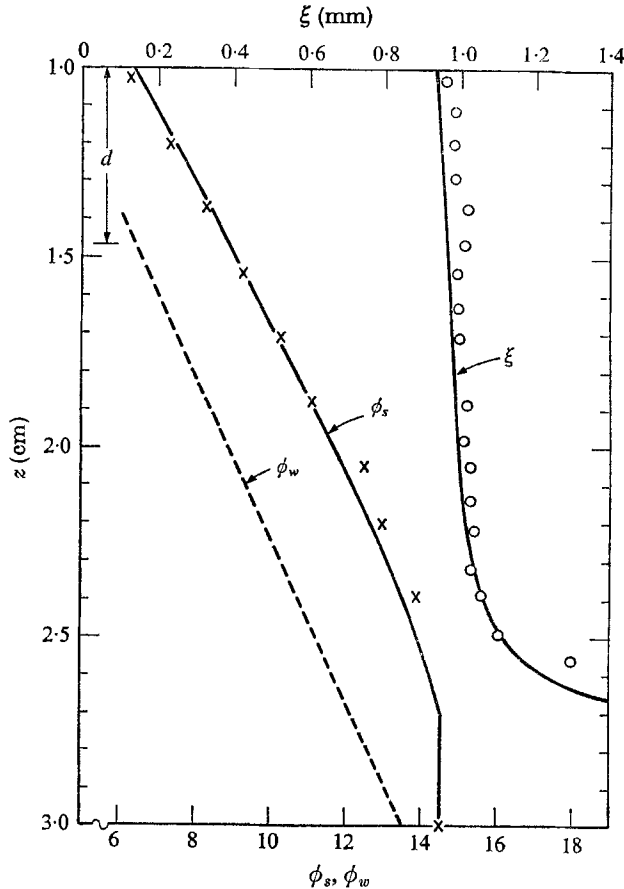

FIGURE 12. Stream radius and potential for the decelerating case of figure 9. ——, predicted by numerical integration of (17) and (24), using as boundary conditions the potential and radius at $z = 1$ cm and the choking condition and potential at the outlet. The choking distance is matched by varying the offset distance d, which is 4·69 mm for the computation, as shown in the figure. Experimental conditions are as given with figure 11.

To avoid entrance effects in comparing observations to predictions using the long-wave model, the position $z = 1$ cm of figure 11 is taken as the entrance, with the radius, stream and wall potentials taken as those measured. The wall potential is then negative, and represented by V_w and an offset distance d (defined in figure 2), which is negative. Numerical integration of (17) and (24) is performed with the downstream boundary conditions represented by the requirements that the flow choke at the outlet and the potential be V_s. This choking distance is a function of the distance d, which is varied to give choking at the outlet. The offset d, arrived at in this way, is within 10 % of the measured value, as shown in figure 12.

The stream potential distribution for decelerating flow characterized by figure 11 shows why the outlet potential V_s must be lowered below V_w to make the flow régime switch from the decelerating to the accelerating mode. The choking at the downstream electrode results in a region over which the potential fall is small. Thus, V_s can be less than V_w, and the stream potential still remain greater than the wall potential over the region between the choking point and the inlet.

6. Concluding remarks

It is clear that many of the steady-flow characteristics of the stream can be predicted using the simple quasi-one-dimensional model. This model helps to explain why the range of fascinating phenomena reported by Taylor (1969 b) is possible. Of course, the price paid here for introducing a potential wall for the purpose of allowing a tractable representation of the shear stress is that the connexion with observations made without the wall is somewhat speculative. The structure does provide a stream control with practical advantages.

Clearly, even the steady-state current-driven jet is as much governed by 'Mach' conditions as by the magnitude and direction of the electrical shear stresses. Instead of the sound velocity, it is the velocity of electrohydrodynamic polarization waves that is critical. Taylor (1959) has shown similar dramatic influences of critical flow on the breakup and shaping of thin liquid sheets. In his studies, a capillary wave system was shown to determine many features of the purely hydrodynamic steady flow configurations.

The model given here should also give meaningful predictions on the dynamic responses, say, of perturbations from the equilibria discussed. Stability of the stream as it is influenced by the equilibrium electrical shear stresses, viscosity, and finite electrical relaxation time, require careful attention.

However, even with the control structure included in the experiment, the domain of validity for the long-wave model in representing stream stability is somewhat restricted. Perturbation wavelengths shorter than $2\pi R$ are likely to be important in determining stability. There is also a subtle restriction on the viscosity. The stream must be sufficiently viscous to justify taking the velocity profile as essentially uniform, if the model developed here is to be valid. But, in our computations, the longitudinal viscous force density (the last term in (16)), is ignored, thus removing the viscosity as an explicit parameter. If we take the longitudinal force as being on the order of ρg, these approximations require, respectively, that $(\mu v/R^2 \ll \rho g \ll \mu v/\xi^2)$. In our experiments, $\mu = 0.36$ kg/m-sec, and typically, the inequalities are satisfied, but with a greater viscosity, the last term in (16) could be important to the steady flow. A lesser viscosity could invalidate the long-wave model. The physical phenomena described in §5 are shown in a newly released educational film (Melcher 1970).

REFERENCES

BASSET, A. B. 1894 *Amer. J. Math.* **16**, 93.

CARSON, R. S. & HENDRICKS, C. D. 1964 *AIAA 4th Electric Propulsion Conf.* Philadelphia, Paper no. 64–675.

COURANT, R. & FRIEDRICHS, K. O. 1948 *Supersonic Flow and Shock Waves.* New York: Interscience.

HEIL, H. & SCOTT, B. W. 1969 *IEEE*, Paper no. 69 C 42 ED, New York.

HOGAN, J. J., CARSON, R. S., SCHNEIDER, M. J. & HENDRICKS, C. D. 1964 *AIAA J.* **2**, 1460.

MELCHER, J. R. 1963 *Field-coupled Surface Waves.* M.I.T.

MELCHER, J. R. & SCHWARZ, W. J. 1968 *Phys. Fluids*, **11**, 2604.

MELCHER, J. R. 1970 *Electric Fields and Moving Media.* Education Development Center, 39, Chapel St., Newton, Mass. 02160: Education Development Center for the National Committee on Electrical Engineering Films.

MILLER, E. P. & SPILLER, L. L. 1964 *Paint and Varnish Production* (June–July).

NAYYER, N. K. & MURTY, G. S. 1960 *Proc. Phys. Soc.* **75**, 369.

PESKIN, R. L., RACO, R. J., YEH, P. S. & MOREHOUSE, J. 1965 *API Res. Conf. Distillate Fuel Combustion*, Paper no. CP65-6-1965.

SAVILLE, D. A. 1971 *Phys. Fluids*, **13**, 2897.

SHAPIRO, A. H. 1953 *Compressible Fluid Flow* (vol. 1). New York: Ronald Press.

STOKER, J. J. 1957 *Water Waves.* New York: Interscience.

SWEET, R. G. 1964 *Stanford Electronics Laboratories*, Stanford, Calif. Pub. no. 1722–1.

TAYLOR, G. I. 1959*a* *Proc. Roy. Soc.* A **253**, 289.

TAYLOR, G. I. 1959*b* *Proc. Roy. Soc.* A **253**, 296.

TAYLOR, G. I. 1959*c* *Proc. Roy. Soc.* A **253**, 313.

TAYLOR, G. I. 1968 *Proc. Roy. Soc.* A **306**, 423.

TAYLOR, G. I. 1969*a* The stability of a fine fluid jet in a longitudinal field. Presented at Int. Symp. Electrohydrodynamics, M.I.T., Cambridge, Mass.

TAYLOR, G. I. 1969*b* *Proc. Roy. Soc.* A **313**, 453.

ZELENY, J. 1917 *Phys. Rev.* **10**, 1.
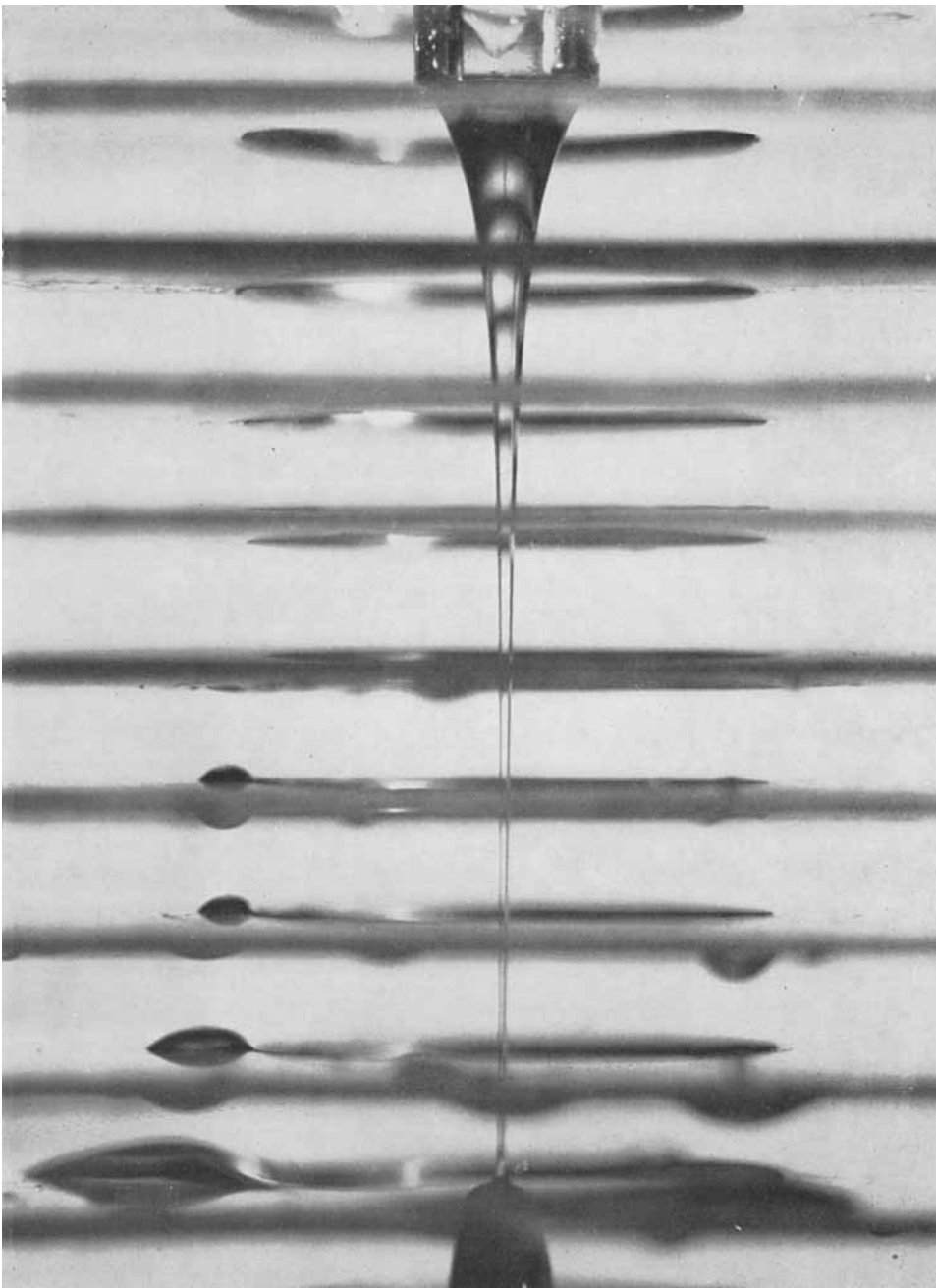
FIGURE 7. Accelerating stream between orifice at top and electrode at bottom. Horizontal lines are the wall electrodes. Without fields, glycerin drips from orifice. Steady flow is established by simultaneously raising V_s and V_w until the stream 'strikes' to the lower electrode. Experimental conditions are those of figure 8.
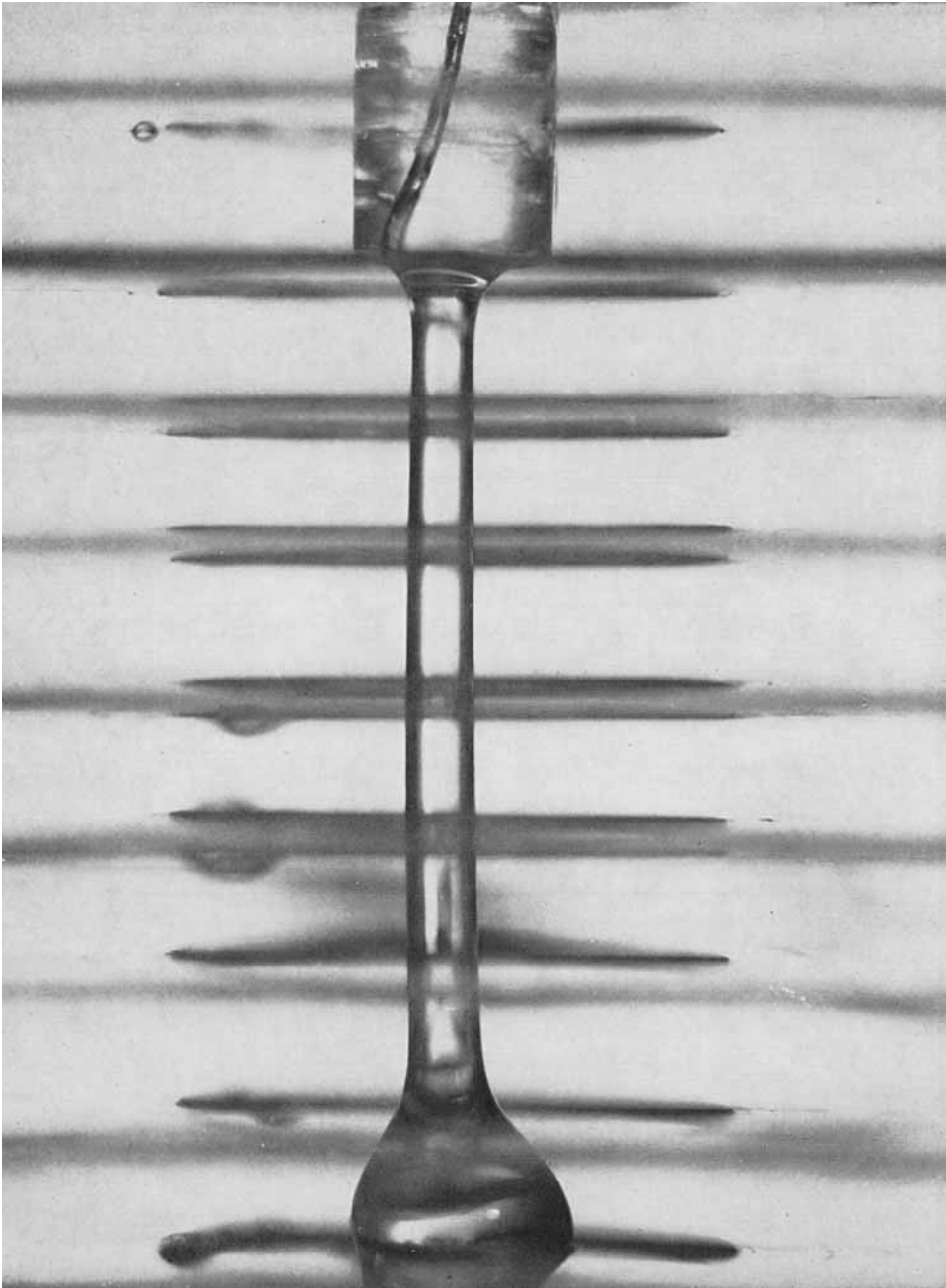
FIGURE 9. Decelerating stream. Orifice is at top with choking evident at the lower electrode. Data as given with figures 11 and 12.